A "virtual-interferometer" technique for surface metrology

Scott M. Jobling[1,*] and Paul G. Kwiat[2]

[1]*Department of Electrical and Computer Engineering, University of Illinois at Urbana-Champaign, 1406 W Green Street, Urbana, IL 61801, USA*

[2]*Department of Physics, University of Illinois at Urbana-Champaign, 1110 W Green Street, Urbana, IL 61801, USA*

**jobling2@illinois.edu*

Abstract: We demonstrate a novel technique for performing aberration-corrected surface metrology within existing wavefront-feedback systems. Our technique uses several phase measurements to calculate phase differences that directly reveal the surface gradients of an object under test, due to orthogonal displacements of that object between measurements. We then apply a least-squares algorithm for surface reconstruction using the gradient information. This approach also removes static system aberrations, providing an absolute measurement of the surface profile. To date, we have profiled a number of test optics with 20- to 40-nm RMS error, where the accuracy is determined by the amount of angular crosstalk over the system aperture.

©2010 Optical Society of America

OCIS codes: (120.3940) Metrology; (120.5050) Phase Measurement.

References and links

1. B. Bowe, and V. Toal, "White light interferometric surface profiler," Appl. Opt. **37**(6), 1796–1799 (1998).
2. H. M. Shang, Y. Y. Hung, W. D. Luo, and F. Chen, "Surface profiling using shearography," Opt. Eng. **39**(1), 23–31 (2000).
3. P. Caber, "Interferometric profiler for rough surfaces," Appl. Opt. **32**(19), 3438–3441 (1993).
4. S. R. McNeill, M. A. Sutton, Z. Miao, and J. Ma, "Measurement of surface profile using digital image correlation," Exp. Mech. **37**(1), 13–20 (1997).
5. S. Bonora, I. Capraro, L. Poletto, M. Romanin, C. Trestino, and P. Villoresi, "Wave front active control by a digital-signal-processor-driven deformable membrane mirror," Rev. Sci. Instrum. **77**(9), 093102 (2006).
6. F. Gonté, A. Courteville, and R. Dändliker, "Optimization of a single-mode fiber coupling efficiency with an adaptive membrane mirror," Opt. Eng. **41**(5), 1073–1076 (2002).
7. T. Weyrauch, M. A. Vorontsov, J. W. Gowens II, and T. G. Bifano, "Fiber coupling with adaptive optics for free-space optical communication," in Proc. of SPIE 4489, 177–184 (2002).
8. L. Zhu, P.-C. Sun, D.-U. Bartsch, W. R. Freeman, and Y. Fainman, "Wave-front generation of Zernike polynomial modes with a micromachined membrane deformable mirror," Appl. Opt. **38**(28), 6019–6026 (1999).
9. W. Southwell, "Wave-front estimation from wave-front slope measurements," J. Opt. Soc. Am. A **70**(8), 998–1006 (1980).

1. Introduction

There are many optical applications that rely on detailed knowledge of surface information for a particular element. For standard optics, this information is often obtained by characterizing the object before use, with any of a number of specialty optical systems or commercial surface profilers [1–4]. Unfortunately, these approaches are not sufficient for optics that must be measured *within* existing optical systems, such as adaptive-optic (AO) devices that have variable surface shapes. However, we show that it is possible to realize in-system, aberration-corrected profilometry without *any* optical modifications, by using precise knowledge of the optical wavefront and precision translation mounts.

Our technique for performing precise in-system metrology alleviates the need to add or remove optics for characterization, and self-corrects for aberrated optical paths in what are often nanometer-sensitive systems. In fact, for many systems that already employ wavefront sensors, the optics and mechanics required for our technique are likely either in place already or involve straightforward and inexpensive modifications.

#124430 - $15.00 USD Received 18 Feb 2010; revised 29 Mar 2010; accepted 31 Mar 2010; published 12 Apr 2010

2. Description

2.1 Virtual interferometer technique

With the goal of performing surface metrology in mind, we first consider a typical interferometric profilometer shown in Fig. 1. In this system, an object under test and a reference object (assumed to be a flat mirror) are imaged onto a CCD camera in order to generate fringes, which result from the difference in surface shape between the object under test and the reference object. Given an algorithm for accurately unwrapping the phase information contained in the fringe pattern, this technique is capable of determining the surface shape of the object under test directly from the measured data; the results are obviously limited by the flatness of the reference object, the sensitivity of the camera, and the stability of the interferometer.

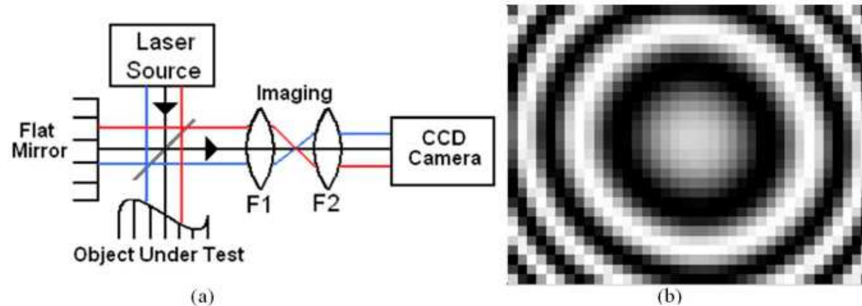

Fig. 1. An interferometric approach for surface metrology. (a) Experimental layout. (b) Example fringe pattern measured by camera.

If we use a wavefront sensor in place of the camera, as shown in Fig. 2, we can treat the system as a *virtual* interferometer (VI), where each arm is measured separately and the results are combined to reveal the surface shape by calculating the wavefront difference. Again, the final result is limited by the quality of the optical path and the reference object.

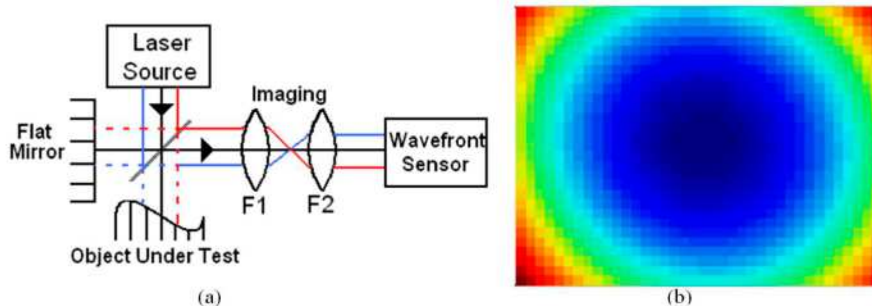

Fig. 2. A virtual-interferometric approach for surface metrology. (a) Experimental layout, in which the wavefront from each arm is measured separately, and the results are subtracted to determine the surface shape of the object under test. (b) Example wavefront difference calculated from individually measured wavefronts.

We are able to obtain surface shape information with either the CCD or VI methods; however, we see that there are two limitations common to both approaches. First, the optical paths for each arm must be identical or exactly known, requiring precise characterization of the reference optic. Second, both approaches require an extra arm to be built into existing systems, which may be inconvenient or impossible due to efficiency or space requirements. We now present a system without these limitations. Consider an alternative single-arm virtual-interferometric (SAVI) approach, shown in Fig. 3, in which the reference arm has been

#124430 - $15.00 USD Received 18 Feb 2010; revised 29 Mar 2010; accepted 31 Mar 2010; published 12 Apr 2010
(C) 2010 OSA

removed. The idea is to measure the surface profile of the object under test using an approach similar to shearing interferometry.

By displacing the object between measurements, we can determine the surface gradient of the object along the direction of displacement (Fig. 4), and thus extract accurate information about the surface. This single-arm approach eliminates the two key disadvantages of the two-arm approaches, i.e., the need for and uncertainty from additional reference optics. Instead, this approach requires only the wavefront sensor and imaging system, as well as the capability to laterally displace the object under test. These components are quite standard, e.g., in adaptive-optic measurement systems. In fact, wavefront sensing has become a vital resource for many applications, most commonly as feedback in AO systems [5,6]. Wavefront flatness, for example, can be used as feedback for optimizing laser focusing and single-mode fiber coupling [5,7], while total wavefront knowledge is required for other applications such as the generation and characterization of Zernike aberrations [8]. The built-in nature of the SAVI technique may enable and/or incentivize its use in particular applications where it may be currently impossible or impractical to include reference optics

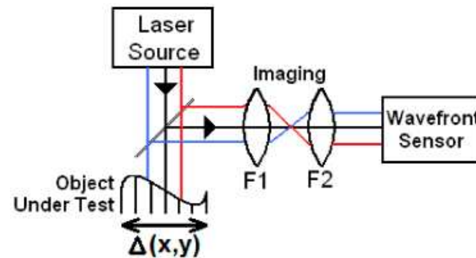

Fig. 3. A single-arm virtual-interferometric approach for surface metrology: F1 and F2 are the focal lengths of lenses arranged in a 4f-imaging configuration, used to image the surface of the object under test onto the wavefront sensor.

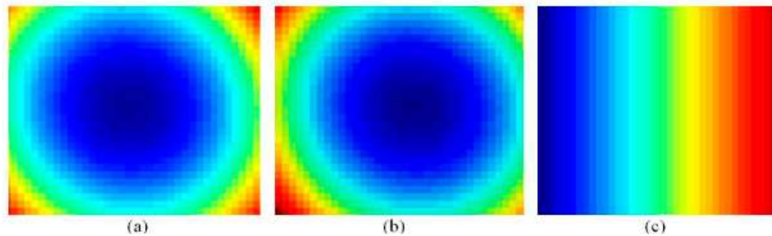

Fig. 4. Displaced-object wavefront measurements. (a) Initial position. (b) Displaced horizontally. (c) Difference between (a) and (b), which corresponds to the gradient of a spherical surface along the direction of displacement.

2.2 Gradient reconstruction

After determining the phase gradient using our SAVI technique, a mathematical integration process is used to reconstruct the surface shape from the measured gradients. The reconstruction algorithm must be tolerant to noisy or invalid data. For example, missing data points (shown as white space in the left corners of the gradient data in Fig. 5) can arise from low illumination or clipping along the beam path. Such errors render straightforward integration ineffective, due to the undetermined contribution missing data would make to the cumulative sum along a given row or column during integration.

#124430 - $15.00 USD Received 18 Feb 2010; revised 29 Mar 2010; accepted 31 Mar 2010; published 12 Apr 2010
(C) 2010 OSA

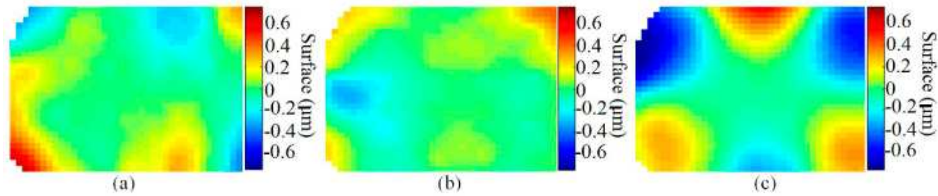

Fig. 5. Experimental gradient reconstruction data for a deformable mirror approximating a trefoil shape. (a) Horizontal gradient. (b) Vertical gradient. (c) Reconstructed surface.

Noisy gradient data can arise from a number of potential sources: actuator displacement and crosstalk errors can each cause mechanical inaccuracy, while instability can be introduced by the movement of any optic within the system between measurements. Additionally, the wavefront sensor may introduce several types of noise, though these errors are device dependent. For example, a Shack-Hartmann sensor may have static and dynamic calibration errors, as well as noise from the CCD array used to measure the slope values. The static calibration errors contribute to the background wavefront removed during the gradient calculation, while the dynamic calibration errors are included in the specification for the wavefront sensor resolution. We decided to implement a best-fit approach designed to minimize the impact of uncorrelated noise, such as the CCD noise; we also include a few preliminary steps to address particular problems with other types of errors.

Since the overall system resolution depends on each step of the reconstruction process, it is important to consider the effect of each source of error in order to adequately address each during reconstruction. As discussed below, we use an iterative, least-squares, best-fit algorithm that produces the "best" surface for a given set of gradient measurements. This approach ignores invalid data and reduces the impact of local slope errors, i.e., the random variations of a single data point, although it does not address errors that impact multiple data points in a correlated manner. Mechanical errors, which result in a displacement or tilt of the entire measured wavefront, must therefore be dealt with separately from the fitting algorithm. Since both the actuator resolution and lateral crosstalk for our XYZ translation stage are significantly less than the spatial resolution of the wavefront sensor (that is, less than 1-µm displacement error compared to 150-µm pixel spacing), and we average each measurement over several trials, we can ignore these errors. However, with a higher-resolution wavefront sensor or larger lateral displacement errors, this assumption may not be justified.

In addition to the lateral crosstalk errors, another form of mechanical error is *angular* crosstalk, which takes the form of tilts about the XYZ axes of the translation stage as a result of displacement along any particular axis. Although these errors are usually quite small, angular crosstalk has a cumulative impact on the reconstruction error due to the integrative nature of the gradient reconstruction process. For example, we have observed repeatable crosstalk tilts on the order of 50 µrad for the typical displacements in our system. This corresponds to a predictable, linearly varying error on the order of 0.5 µm over a 20-mm aperture, which is added to the gradient data. If left unchecked, this error would accumulate during reconstruction and imply a false curvature along each axis with a peak-to-valley amplitude of 2.5 µm, or roughly the same as a 20-m spherical mirror! Given the predictable nature of the crosstalk, we opted to measure and remove the tilt bias for each displacement, effectively reducing the 50-µrad tilts to less than 2 µrad. This approach is limited by the tilt measurement accuracy, and is discussed in more detail in Section 4.

After removing all global errors, we can move forward with the gradient reconstruction process. Building on the similarities between this technique and shearing interferometry, we have chosen a modified version of the shearing-interferometer reconstruction process detailed by Southwell in [9], supplemented with a few additional steps. To begin, we subtract off a few low-order surface shapes that can be calculated directly from the gradient data in a robust manner; they will be added back in at the end of the iterative reconstruction. This initial step lets us quickly isolate the lowest-spatial-frequency and typically largest-amplitude components from the gradient data. The low spatial-frequency components are the most

#124430 - $15.00 USD Received 18 Feb 2010; revised 29 Mar 2010; accepted 31 Mar 2010; published 12 Apr 2010
(C) 2010 OSA

problematic for our algorithm since it only considers a few local data points at a time; thus, removing the low-order terms ahead of time can greatly improve the performance of the iterative fitting step. We subtract several low-order terms, C , from the measured gradients, $\nabla_{x,y}\phi$, via projection onto a finite basis of known gradients, A , as shown in Eqs. (1-3):

$$(C)=\begin{pmatrix}\nabla_x\phi\\ \nabla_y\phi\end{pmatrix}\times(A), \text{ and} \tag{1}$$

$$\begin{pmatrix}\nabla_x\phi'\\ \nabla_y\phi'\end{pmatrix}=\begin{pmatrix}\nabla_x\phi\\ \nabla_y\phi\end{pmatrix}-(C)\times\left(A^T\right), \text{ where} \tag{2}$$

$$(A)=\begin{pmatrix}\nabla_x\phi_{Tilt0^\circ} & \nabla_x\phi_{Tilt90^\circ} & \nabla_x\phi_{Astig0^\circ} & \nabla_x\phi_{Astig45^\circ} & \nabla_x\phi_{Foc}\\ \nabla_y\phi_{Tilt0^\circ} & \nabla_y\phi_{Tilt90^\circ} & \nabla_y\phi_{Astig0^\circ} & \nabla_y\phi_{Astig45^\circ} & \nabla_y\phi_{Foc}\end{pmatrix}, \text{ and} \tag{3}$$

$\nabla_{(x,y)}\phi_{(Z)}$ refer to the horizontal and vertical gradients of five Zernike terms: tilt (horizontal and vertical), astigmatism (horizontal and diagonal), and focus. We have chosen to subtract the tilt, astigmatism, and focus terms, since each can be readily expressed in terms of Zernike or Legendre polynomials, depending on the system aperture. The resulting set of coefficients, C , is saved so we can add the terms back into the surface data later; the resulting reduced amplitudes of the updated gradients, $\nabla_x\phi'$ and $\nabla_y\phi'$, help to improve the speed and accuracy of the best-fit algorithm. If the system aperture is not exactly circular or rectangular, the chosen basis functions may not be orthogonal over the given aperture. To work around slightly non-orthogonal basis functions, we apply this projection term-by-term over a few cycles. By subtracting the calculated amplitude for each term from the gradient data before evaluating the overlap with the next term, we iteratively project the residual slopes onto the basis functions, which generally converge to a fixed set of coefficients after several iterations. This approach allows us to avoid having to ignore data or continually adjust the basis functions in order to maintain orthogonality.

Next, we use Southwell's algorithm to calculate the best-fit surface shape from the residual gradients calculated in the previous steps. Other than using surface gradients rather than wavefront slopes, the iterative process is identical to the original implementation. The algorithm calculates an initial array of local surface deviations, $b_{j,k}$, for each pair of indices, j and k , using the surrounding horizontal and vertical gradient values. Using these local surface deviations as a fixed reference, the algorithm then updates the ith current surface estimate, $\phi^i_{j,k}$, using an iteratively updated local average, $\bar{\phi}^i_{j,k}$, and the fixed local deviation, which sum to the actual surface value once converged. Also, each term is weighted by $w_{j,k}$, $w_{\bar{\phi}_{jk}}$, or $w_{b_{jk}}$ in order to handle missing or invalid data points. More specifically, $w_{j,k}$ indicates whether the current indices refer to a valid point, $w_{\bar{\phi}_{jk}}$ is the inverse of the total number of valid points considered in the phase-average calculation, and $w_{b_{jk}}$ depends on the desired algorithm behavior for calculating local deviations at the aperture border and around invalid data points. This process is summarized in Eqs. (4-6):

$$\phi^i_{j,k}=\bar{\phi}^i_{j,k}+w_{j,k}b^i_{j,k}, \text{ and} \tag{4}$$

$$\bar{\phi}^i_{j,k}=w_{\bar{\phi}_{jk}}(\phi^i_{j+1,k}+\phi^i_{j,k+1}+\phi^i_{j-1,k}+\phi^i_{j,k-1}), \tag{5}$$

$$b^i_{j,k}=w_{b_{jk}}(\nabla_y\phi^i_{j-1,k}-\nabla_y\phi^i_{j,k}+\nabla_x\phi^i_{j,k-1}-\nabla_x\phi^i_{j,k}). \tag{6}$$

#124430 - $15.00 USD Received 18 Feb 2010; revised 29 Mar 2010; accepted 31 Mar 2010; published 12 Apr 2010
(C) 2010 OSA

Once the iterative best-fit step is complete, we again subtract off several low-order surface shapes from the residual surface estimate. Since the low-order terms were removed before reconstruction, we know that any terms which are present after the reconstruction are erroneous artifacts of the reconstruction algorithm itself and should be ignored. Finally, we add the correct low-order terms back onto the reconstructed surface shape, and apply a scaling factor determined by whether the object is reflective or transmissive: for reflective objects, the angle of reflection is twice the actual value of the surface normal angle, while for transmissive objects this scale factor is 1.

2.3 Experiment components

In order to demonstrate the SAVI technique, we simply adapted an existing system that used a Shack-Hartmann wavefront sensor (Haso32) for adaptive-optic (AO) feedback. Since the original AO system required accurate phase information and precise alignment, the necessary imaging and translation capabilities were already built in. Depending on the desired aperture, we used either a 200:60 mm or 200:100 mm 4-f imaging system with achromatic lenses for F1 and F2 in Fig. 3. For a 4-f imaging system, the lenses are separated by the sum of the two focal lengths, and F1 (F2) is placed a focal length away from the object (image) plane. The system magnification is equivalent to the ratio of the two focal lengths, or roughly 3:1 and 2:1 for our two configurations: based on the wavefront sensor array size, which is 6.0 x 4.8 mm^2, the maximum measurable aperture was thus either 20 x 16 mm^2 or 12 x 9.6 mm^2. An XYZ stage with 1-μm Vernier resolution was used to displace the object under test; the stage had a predictable 30-50 μrad of angular crosstalk over the region of interest. Also, we matched the displacement distance through the imaging system with the 150-μm pixel spacing of the wavefront sensor, resulting in either a 450- or 300-μm object displacement between measurements. This provides the highest possible system resolution while minimizing the effect of translation errors, as outlined in the discussion section.

3. Results

3.1 Characterizing optical elements

To evaluate the profiling capabilities of the virtual-interferometer technique, we characterized one-inch flat and spherical mirrors. The measured profiles are shown in Fig. 6.

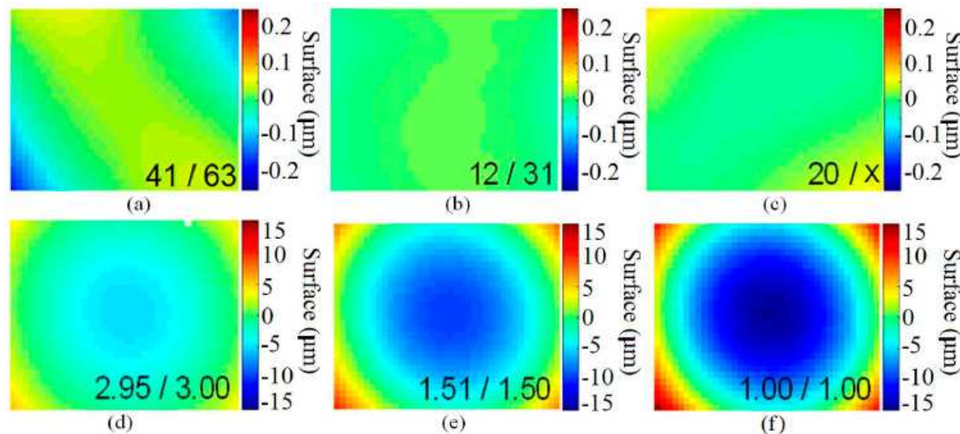

Fig. 6. Surface data for various optical elements. Each measurement used the 200:100-mm imaging system, with a maximum aperture of 12x9.6 mm^2. The numbers on the plots indicate the measured / specified parameters for each element (X indicating unknown). (a-c) Flat mirror profiles and RMS-flatness data in nanometers. Note: specified value is a maximum tolerance. (d-e) Spherical mirror profiles and radius of curvature data in meters.

Two of the flat mirrors had a maximum tolerance of $\lambda/10$ and $\lambda/20$ flat, at a wavelength of 633 nm, respectively; we found that both of these were within acceptable

#124430 - $15.00 USD Received 18 Feb 2010; revised 29 Mar 2010; accepted 31 Mar 2010; published 12 Apr 2010
(C) 2010 OSA

tolerances over the measured aperture, and the third mirror (whose specified flatness is unknown) was comparably flat. We found the curvatures of the measured spherical mirrors to be close to each of the quoted values, and confirmed the specifications directly using deflections of a laser beam off various locations on the mirror surface. For the three spherical mirrors, we found 2.94 m, 1.49 m, and 1.00 m, in excellent agreement with the SAVI measurements.

3.2 Removal of background aberrations

In order to demonstrate the aberration-correction capabilities of the SAVI technique, we used a standard microscope slide to introduce aberrations into the object beam path, thereby distorting the wavefront sensor measurements. If the system were using a reference arm for comparison, these aberrations would appear to be part of the object under test, and would be erroneously added onto the surface profile. Instead, we observed near total removal of the aberrations. While we did find some small deviations between the two reconstructions, the difference was lower than our estimated 40-nm RMS system resolution for the imaging optics in place. The reconstruction results for both the unaberrated and aberrated cases are shown in Fig. 7.

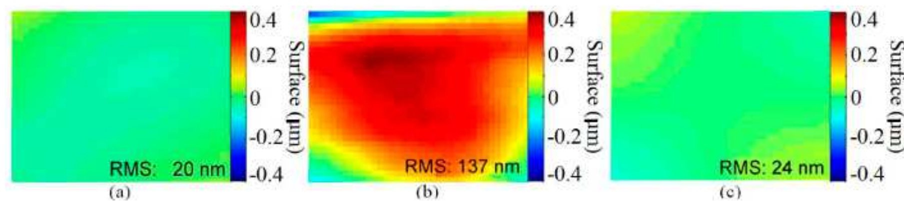

Fig. 7. Demonstration of background removal with the SAVI technique. (a) Flat mirror reconstructed with unaberrated beam path. (b) Measured aberrations added to beam path by a microscope slide. (c) Flat mirror reconstructed with aberrated beam path.

4. Discussion and conclusions

There were several issues we had to address in order to make the system reliable. In order to help compensate for both the system instability between measurements and slight displacement error, we made several repeated measurements for each gradient calculation. Also, we had to carefully characterize the angular crosstalk of the displacement stage; as mentioned in Section 2, any false tilt data would generate false curvature estimates. Since astigmatism and focus are the only terms that can be completely and mutually described by positive and negative curvatures, these are the only aberration terms affected by the tilt crosstalk. It should also be noted that the ability of the system to remove static background aberrations is limited to aberrations that do not disrupt the linearity of the system imaging. More specifically, any measured change in phase at the wavefront sensor must be linearly proportional to the actual change in phase at the surface of the object within some finite resolution. Although it is impossible to create a perfect image with physical optics, there will be some resolution below which the imperfections are inconsequential. In our system, for example, the average phase over a single pixel at the wavefront sensor must accurately represent the average phase over the imaged area at the object; thus the wavefront sensor (with 150x150-μm^2 spatial- and $\lambda/150$ phase-resolution) determines the minimum cutoff for imaging performance. There may be other system- or equipment-dependent features which interfere with the imaging performance as well, such as the potential breakdown of Shack-Hartmann wavefront sensors due to too-dim or too-bright illumination, high spatial-frequency components ($\pm$ 3° slopes for our sensor), the specified accuracy of the wavefront sensor, or even beam clipping within the optical system as a result of large focus values. Additionally, the surface to be reconstructed must be well sampled by the wavefront sensor.

Our measurement accuracy is presently limited by the angular crosstalk encountered during lateral displacement of the object under test. Although an optimal solution would be to

#124430 - $15.00 USD Received 18 Feb 2010; revised 29 Mar 2010; accepted 31 Mar 2010; published 12 Apr 2010
(C) 2010 OSA

utilize a translation stage with sufficiently low crosstalk, this is not always practical. In order to compensate for these errors in our system, for example, we determined the translation stage crosstalk by measuring the horizontal and vertical curvature of several flat mirrors, and then removed the crosstalk mathematically prior to running the reconstruction algorithm. Trusting the flatness specification for each mirror, we know that any measured values larger than the given tolerance are a result of the crosstalk. More specifically, by measuring the average curvatures of several flat mirrors known to be better than $\lambda/10$ (63-nm RMS) flat over a 1-inch aperture, we can isolate any crosstalk bias that implies a curvature larger than allowed by the tolerance. Based on the largest curvatures allowed over the maximum apertures for the two imaging configurations, we have estimated our system resolution to be 20- to 40-nm RMS. Furthermore, since both errors due to the angular crosstalk of the stage and our method for removing them involve only global surface curvatures, i.e., focus and astigmatism, these errors only impact the estimates of the focus and astigmatism components of the reconstructed surface.

Overall, we expect that the system is capable of matching our current wavefront sensor resolution, i.e., as low as 5-nm RMS errors with 150-μm lateral pixel spacing at the image plane (which may be higher or lower lateral resolution at the object, depending on the imaging system). The wavefront sensor represents a fundamental "upper-limit" to the performance for our current integrative technique, and the actual system resolution is a product of the displacement distance and sensor resolution. The measured data is averaged over each sensor pixel and scaled according to the displacement distance relative to the pixel size. This implies that smaller displacements require that the measured gradients (noise included) be amplified to match the sensor resolution. On the other hand, this also implies that larger displacements de-emphasize issues with noise in the system. Stated differently, because our technique relies on nearest-neighbor gradient data for calculating surface information, we cannot increase the resolution beyond that of the gradient data, and if we displace the object under test by a distance that is smaller than the sampling resolution, we must amplify both the gradient and noise data to recover the surface shape.

Because our technique relies on measuring surface gradients, obviously only components with measurable gradients can be reconstructed. For example, since typical wavefront-sensing techniques cannot measure constant wavefront offsets, both the offset (piston) and the global tilt components of the surface are lost during reconstruction. Lastly, although our wavefront sensor sets a fundamental limit for system resolution, moving to a higher resolution wavefront sensor would not necessarily improve system resolution. As mentioned earlier, we have been able to ignore several sources of displacement errors and have attainable imaging requirements as a result of the wavefront sensor resolution. Moving from 150-μm to 10-μm pixel spacing, or from $\lambda/150$ to $\lambda/1000$ phase-resolution, which is comparable to many commercial surface profilers, could dramatically increase the difficulty in obtaining wavefront-sensor-limited performance, possibly removing any incentive for performing the surface analysis in-system.

It is worthwhile mentioning that many of the factors that impact our system resolution (i.e., alignment, imaging, sampling, etc.) are also generally designed into the specifications of commercial surface profilers so that the end-user does not need to consider each individually. For example, a precision interferometer-based CCD profilometer with 10-μm pixel spacing may be capable of up to $\lambda/1000$ phase-resolution based on the CCD, but may require specialty calibration to improve over a default $\lambda/20$ resolution based on the optics alone (this example is based on actual specified performance values for optical characterization provided by CVI Melles-Griot). Since our technique can be configured with many different combinations of equipment, ultimately determined by the user, we can only specify the resolution for our particular design. It is essential to consider the set of hardware as a whole when evaluating system resolution for a different layout. We have outlined what we believe to be all the information required to implement the SAVI technique, as well as several device-

#124430 - $15.00 USD Received 18 Feb 2010; revised 29 Mar 2010; accepted 31 Mar 2010; published 12 Apr 2010
(C) 2010 OSA

specific modifications to address particular issues such as noisy data, angular crosstalk, and aberrated optical paths.

In summary, we have demonstrated the ability to perform aberration-corrected in-system metrology through the use of a novel differential gradient virtual-interferometer technique. Although there are profilometers with comparable or better resolution, the ability to perform aberration-corrected metrology within existing systems makes this technique attractive for AO and other wavefront-feedback applications in which the object under test is best measured without removal.

Acknowledgements

We would like to acknowledge helpful discussions with Imagine Optic on wavefront reconstruction techniques, which carried over to this work. This work was supported by the Army Research Office (ARO) MURI W911NF-09-1-0406, and the Intelligence Advanced Research Projects Activity (IARPA) under ARO Contract No. W911NF-05-1-0397.

#124430 - $15.00 USD Received 18 Feb 2010; revised 29 Mar 2010; accepted 31 Mar 2010; published 12 Apr 2010
(C) 2010 OSA